Supporting information

Nacre-inspired strong nanopapers of aramid nanofibers integrated montmorillonite nanoplates, cellulose nanofibrils, and Ag nanowires for high-performance electrical heater

Fugang Hu [a,b], Jinsong Zeng [a,b,*], Pengfei Li [a,b c,*], Tianguang Wang [a,b], Jinpeng Li [a,b], Bin Wang [a,b], Kefu Chen [a,b]

a Plant Fiber Material Science Research Center, State Key Laboratory of Pulp and Paper Engineering, South China University of Technology, Guangzhou, 510640, China

b Guangdong Provincial Key Laboratory of Plant Resources Biorefinery, Guangzhou, 510006, China

c School of Environment and Energy, South China University of Technology, Guangzhou 510640, P.R. China

Corresponding authors:

*Jinsong Zeng, E-mail: fezengjs@scut.edu.cn

*Pengfei Li, E-mail: felpf@scut.edu.cn

Calculations of electromagnetic shielding interference effectiveness

The transmission (T), reflection (R), and absorption (A) were calculated based on the scattering parameters (S_{11} and S_{21}). The total EMI SE (SE_T), reflection (SE_R), absorption (SE_A), and multiple internal reflections (SE_M) were calculated as follows:

$$R = |S_{11}|^2 = |S_{22}|^2 , T = |S_{12}|^2 = |S_{21}|^2 \quad (1)$$

$$A = 1 - R - T \quad (2)$$

$$SE_R = -10\ log(1 - R) , SE_A = -10\ log(\frac{T}{1 - R}) \quad (3)$$

$$SE_T = SE_A + SE_R + SE_M \quad (4)$$

Where the SE_M is negligible if the SE_T is greater than 10 dB. To compare the effectiveness of shielding materials equitably, EMI SE/t is normalized. Besides, specific shielding effectiveness (SSE) and SSE/t taking into account the density and thickness are represented as follows:

$$SSE = \frac{EMI\ SE}{density} = dB{\cdot}cm^3/g \quad (5)$$

$$SSE/t = \frac{SSE}{thickness} = dB{\cdot}cm^2/g \quad (6)$$

EMI shielding efficiency (%), referring to the capability to block waves in terms of percentage, is obtained using the equation:

$$Shielding\ efficiency\ (\%) = 100 - (\frac{1}{10^{\frac{SE}{10}}}) \times 100 \quad (7)$$

Sample preparation for AFM characterization of ANF and ANF/MTM/CNF composite morphology

Firstly, 150 g of the ANF&DMSO-0.18 suspensions was reprotonated with 150 mL of deionized

water. The reprotonated ANF&DMSO/H_2O suspensions were homogenized by a high-speed kitchen blender (L18-Y38, Joyouny, China) for 2 min, followed with ultrasonication for 3 min with an ultrasonic generator (vcx800, Sonics, USA, 800 W). The nylon membranes with a pore size of 0.22 μm and a diameter of 75 mm were used to vacuum filtrate the reprotonated ANF&DMSO/H_2O suspensions. During the vacuum filtration process, the reprotonated ANF&DMSO/H_2O suspensions were continuously stirred using a glass rod to maintain their dispersion. As the suspensions gradually became viscous, 300 mL of deionized water was added and the filtration continued. Subsequently, when the suspensions became viscous again, another 300 mL of deionized water was added to further wash and remove the DMSO from the suspensions. This process of adding water and washing by vacuum filtration was repeated five times, and the collected suspension was the obtained ANF&H_2O suspensions.

For the preparation of the ANF/MTM/CNF&H_2O suspensions, firstly, MTM&H_2O-0.5 suspensions with a weight percentage of 3.0 wt% were added to 100 mL of DMSO, followed by magnetic stirring for 1 hour, in which the obtained suspensions were called as MTM&DMSO/H_2O suspensions. Meanwhile, the CNF&H_2O-0.5 suspensions with a weight percentage of 2.0 wt% were dispersed into 50 mL DMSO and were also stirred for 1 h, and the suspensions were called as CNF&DMSO/H_2O suspensions. And, the ANF&DMSO-0.18 suspensions were firstly added into the MTM&DMSO/H_2O suspensions, and followed by magnetically stirring for 2 h, where the obtained suspensions were called as ANF/MTM&DMSO/H_2O suspensions. Then, the CNF&DMSO/H_2O suspensions were added into the ANF/MTM&DMSO/H_2O suspensions, and the obtained composite suspensions were stirred for another 2 h, in which the obtained suspensions were called as ANF/MTM/CNF&DMSO/H_2O suspensions. Finally, upon reprotonation, homogenization,

ultrasonication, washing by vacuum filtration, the ANF/MTM/CNF&H_2O suspensions were produced.

The obtained ANF&H_2O and ANF/MTM/CNF&H_2O suspensions were further diluted to a solid concentration of 10^{-5} wt%. Then, the diluted suspensions were dropped onto a mica substrate, and allowed to dry at room temperature for 24 hours. After drying, the samples were ready for AFM characterization.

Sample preparation for cross-sectional observation of nanopapers

In order to preserve the microstructure of the nanopaper during cross-sectional observations, a freezing treatment using liquid nitrogen was conducted for 30 minutes. Subsequently, the nanopaper was manually pulled apart to create a well-defined cross-sectional view. Prior to the liquid nitrogen freezing, a notch was carefully made on the nanopaper using scissors to create a stress concentration point, which helps prevent possible fiber slippage and preserve the original microstructure of the nanopaper during the stretching process.

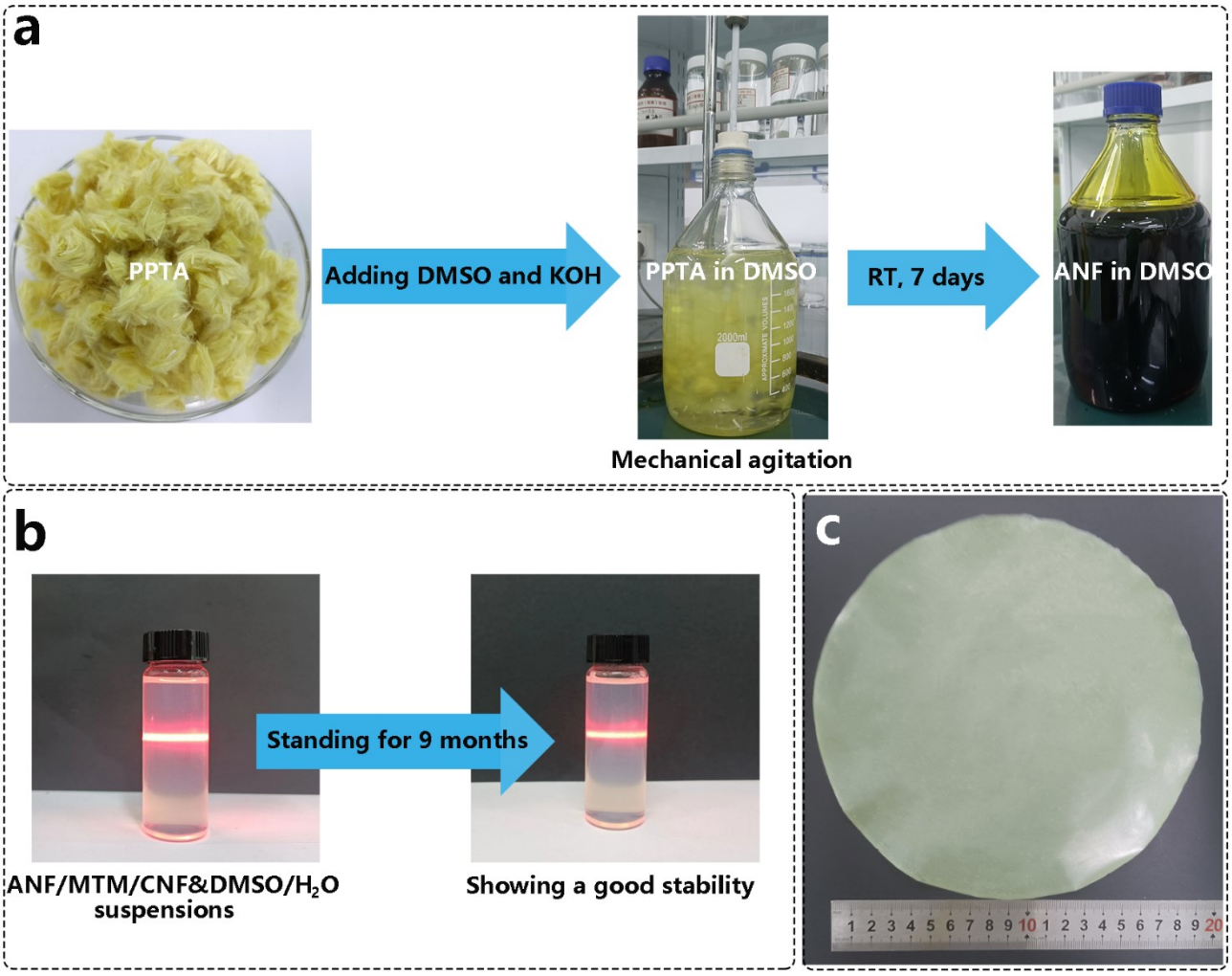

Figure.S1 (a) Schematic description of the preparation process of ANFs. (b) ANF/MTM/CNF&DMSO/H_2O suspensions showing a good stability. (c) A large-sized ANF/MTM/CNF/AgNW-0.2 nanopaper prepared using an automatic papermaking system (RK3AKWT, Austria).

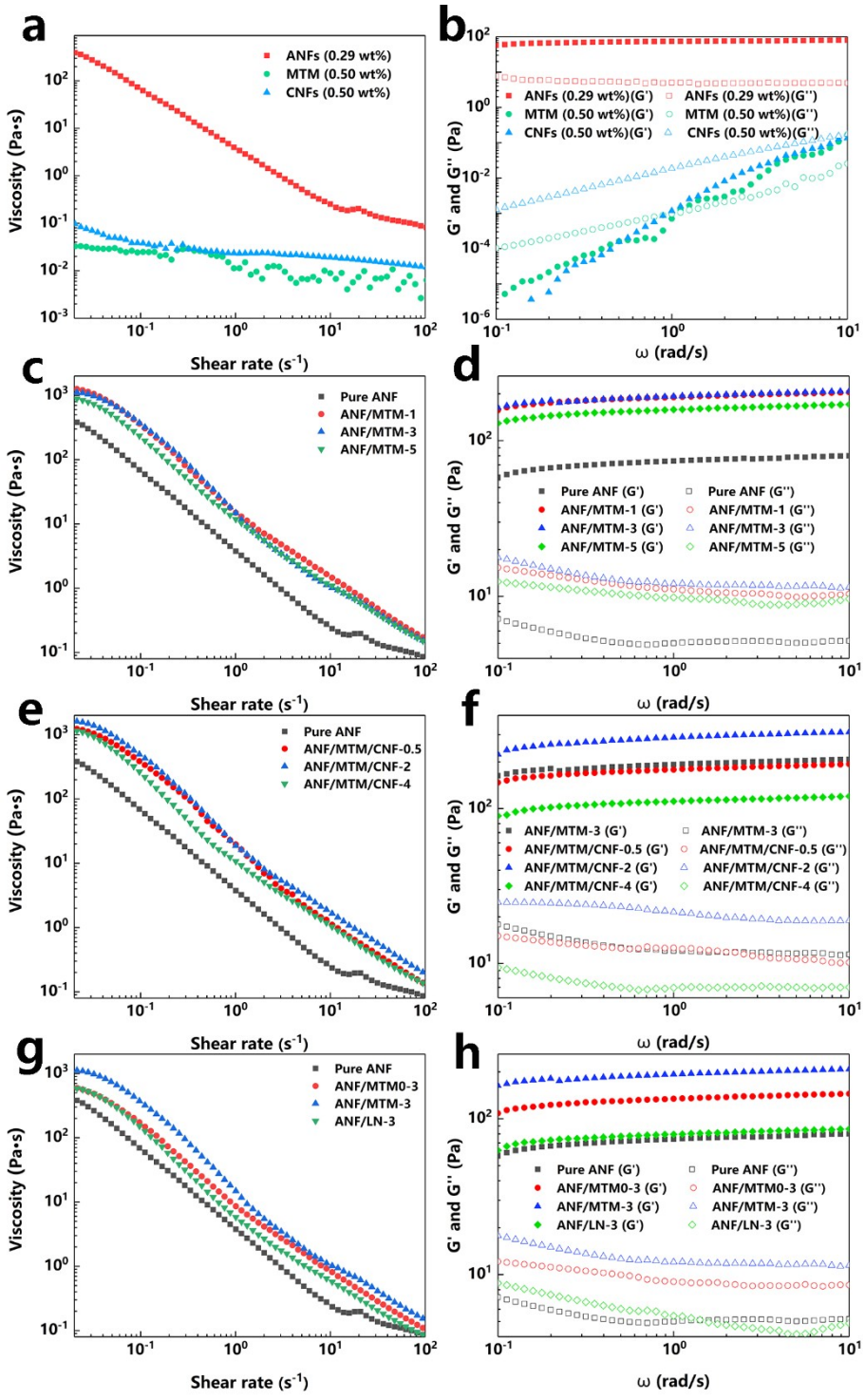

Figure.S2 (a) Shear rate-viscosity curve of the pure ANF, CNF and MTM nanoplate aqueous suspension. (b) Storage modulus G′ (solid symbols) and loss modulus G″ (open symbols) of the pure ANF, CNF and MTM nanoplate aqueous suspension versus angular frequency ω at 25 °C. (c) Shear rate-viscosity curve of the pure ANF, ANF/MTM aqueous suspension. (d) Storage modulus G′ (solid symbols) and loss modulus G″ (open symbols) of the pure ANF,

ANF/MTM aqueous suspension versus angular frequency ω at 25 °C. (e) Shear rate-viscosity curve of the pure ANF, ANF/MTM/CNF aqueous suspension. (f) Storage modulus G′ (solid symbols) and loss modulus G″ (open symbols) of the pure ANF, ANF/MTM/CNF aqueous suspension versus angular frequency ω at 25 °C. (g) Shear rate-viscosity curve of the pure ANF, ANF/MTM0-3, ANF/MTM-3, and ANF/LN-3 aqueous suspension. (h) Storage modulus G′ (solid symbols) and loss modulus G″ (open symbols) of the pure ANF, ANF/MTM0-3, ANF/MTM-3, and ANF/LN-3 aqueous suspension versus angular frequency ω at 25 °C.

Before investigating the synergistic reinforcement of MTM nanoplates and CNFs, three different types of nanoclays were introduced into the ANF framework to identify the most effective nanoclay for reinforcement. These three types of nanoclays included original MTM, MTM modified with cetyl trimethyl ammonium bromide (CTAB), and laponite (LN). For two different MTM, the original MTM was labeled as MTM0 and the MTM modified with CTAB was labeled as MTM directly. MTM0 nanoplates were also prepared by ultrasonication, and the procedure was the same as for the MTM nanoplates modified with CTAB. Meanwhile, LN had no need for additional stripping due to their small original size with diameter in the range of 25-30 nm and thickness of 1 nm (**Fig. S4b**).[1] The preparation of ANF/MTM0 and ANF/LN nanopapers was based on the process of ANF/MTM nanopapers, that was described in the experimental section. As shown in **Fig. S3**, with the introduction of MTM0 and LN nanoplates, the ANF-based nanopapers showed a marked improvement in their mechanical properties. The ANF/MTM0 and ANF/LN nanopapers exhibited the best mechanical properties when incorporating 3 wt% of MTM0 and LN nanoplates, respectively, similar to the MTM nanopapers. As shown in **Table S2**, the δ_c, E_c, ε_c, and U_c of the ANF/MTM0-3 were 399.00 ± 11.18 MPa, 6.81 ± 0.47 GPa, 21.41 ± 1.85%, and 53.76 ± 4.34 MJ/m^3, and the δ_c, E_c, ε_c, and U_c of the

ANF/LN-3 were 401.39 ± 15.31 MPa, 7.94 ± 0.35 GPa, 17.27 ± 1.81%, and 47.72 ± 3.44 MJ/m^3. Overall, the mechanical properties of ANF/MTM-3 nanopapers were superior to the ANF/MTM0-3 and ANF/LN-3 nanopapers (**Fig. S3c**). For LN nanoplates, MTM0 and MTM nanoplates had a higher aspect ratio, providing better stress transfer to the ANF network. Meanwhile, MTM0 and MTM nanoplates had a similar morphology, but the MTM nanoplates had a better reinforced effect, which could be attributed to the excessive hydrophilicity of MTM0 nanoplates. As shown in **Fig. S4**, the contact angle of ANFs was 69.0°. However, the MTM0 nanoplates were completely moistened by water with a contact angle of 0.0°. The significant difference in hydrophilicity between ANFs and MTM0 nanoplates could affect their compatibility with each other. Because of the introduction of CTAB, MTM nanoplates had a higher hydrophobicity and a better compatibility with ANFs, resulting in better mechanical properties of ANF/MTM nanopapers. The rheological properties of ANF/MTM0, ANF/MTM, and ANF/LN suspensions were characterized to study the compatibility and bonding between the components in these suspensions (**Fig. S2)**. As shown in **Fig. S2g** and **h**, compared to the ANF/MTM0-3 and ANF/LN-3 suspensions, the ANF/MTM-3 suspensions had the highest viscosity, storage modulus (G') and loss modulus (G''), demonstrating the better compatibility and bonding between ANFs and MTM nanoplates. Due to the favorable compatibility, MTM nanoplates were able to disperse more uniformly in suspensions and nanopapers, leading to an enhanced interfacial bonding force with ANFs. As a result, the suspensions exhibited higher viscosity, G', and G", while the nanopapers showed improved mechanical properties.

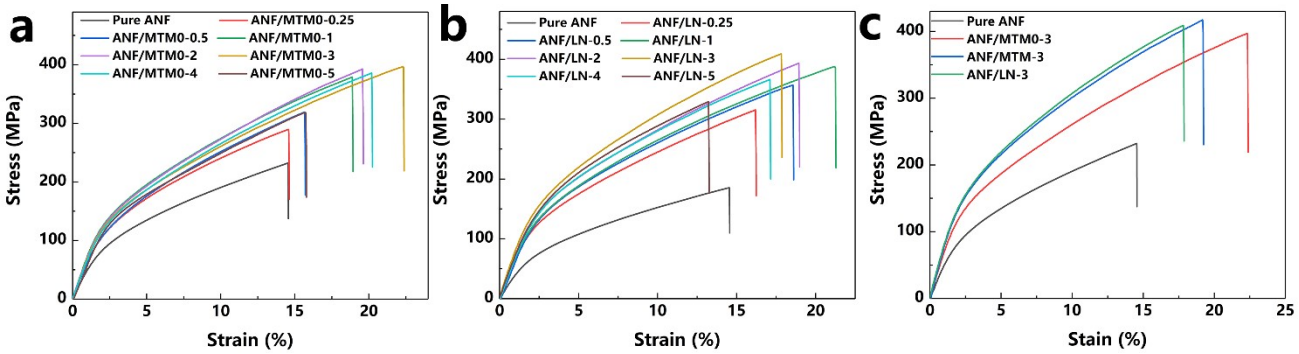

Figure.S3 (a) Stress-strain curves of the pure ANF and ANF/MTM0 nanopapers. (b) Stress-strain curves of the pure ANF and ANF/LN nanopapers. (c) Stress-strain curves of the pure ANF, ANF/MTM0-3, ANF/MTM-3 and ANF/LN-3 nanopapers.

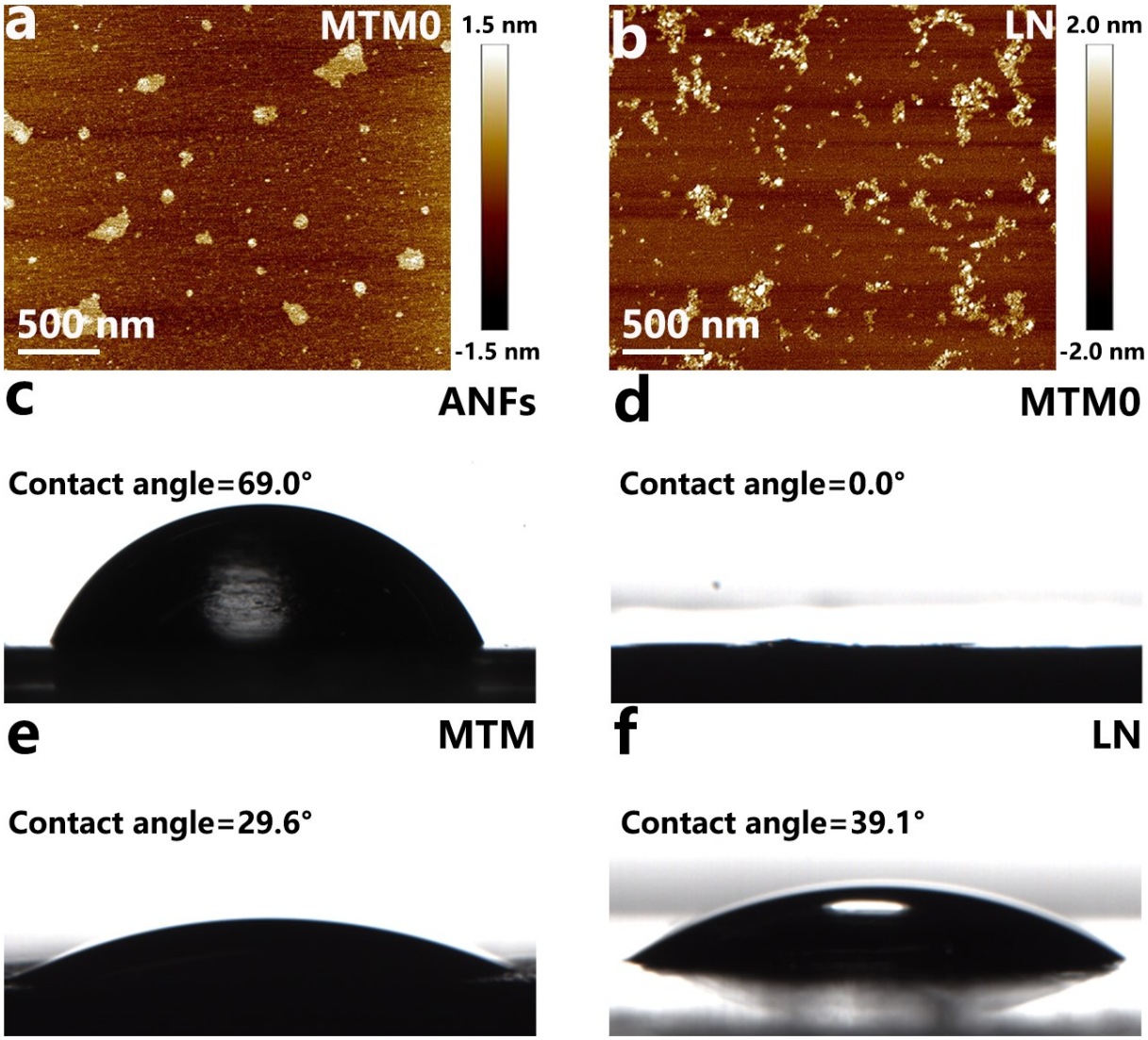

Figure.S4 (a-b) AFM images of (a) MTM0 and (b) LN nanoplates. (c-f) The images of contact angle of (c) ANFs, (d) MTM0 nanoplates, (e) MTM nanoplates, and (f) LN nanoplates.

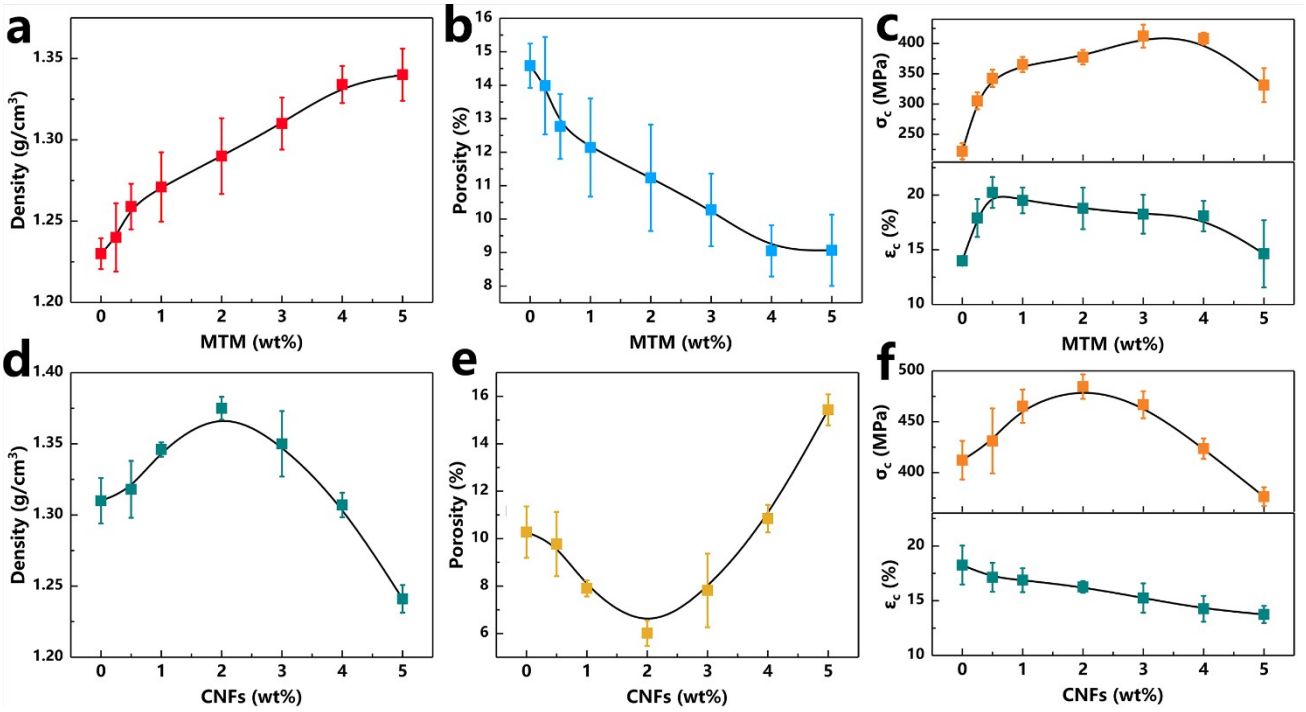

Figure.S5 (a-b) The influence of the weight ratio of MTM nanoplates on the (a) density and (b) porosity of ANF/MTM nanopapers. (c) Tensile stress (δ_c) and elongation (ε_c) as a function of weight ratio of MTM nanoplates to ANFs. (d-e) The influence of the weight ratio of CNFs on the (d) density and (e) porosity of ANF/MTM/CNF nanopapers. (f) Tensile stress (δ_c) and elongation (ε_c) as a function of weight ratio of CNFs to ANF/MTM-3 composite.

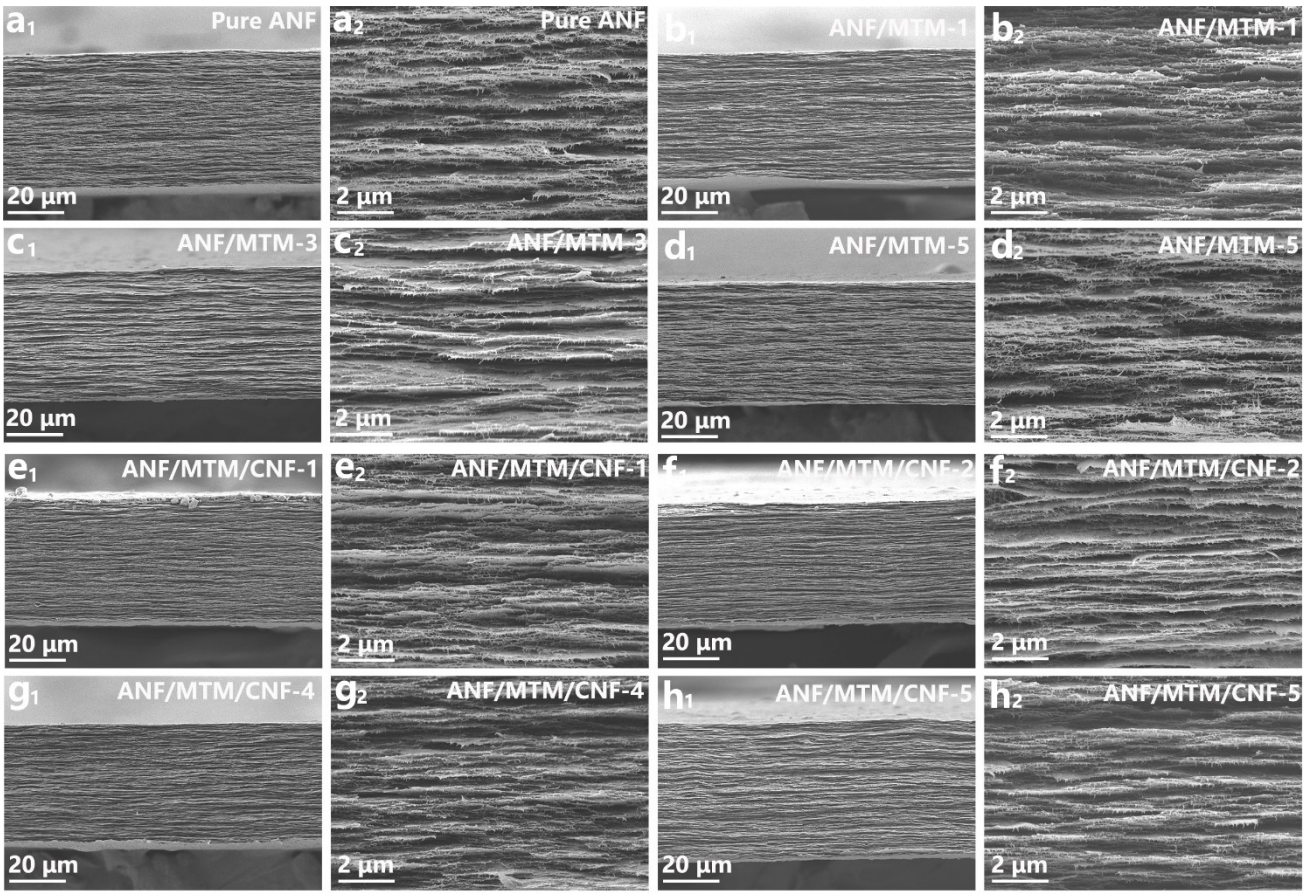

Figure S6 The cross-sectional microstructure of the pure ANF (a), ANF/MTM (b-d), and ANF/MTM/CNF (e-h) nanopapers.

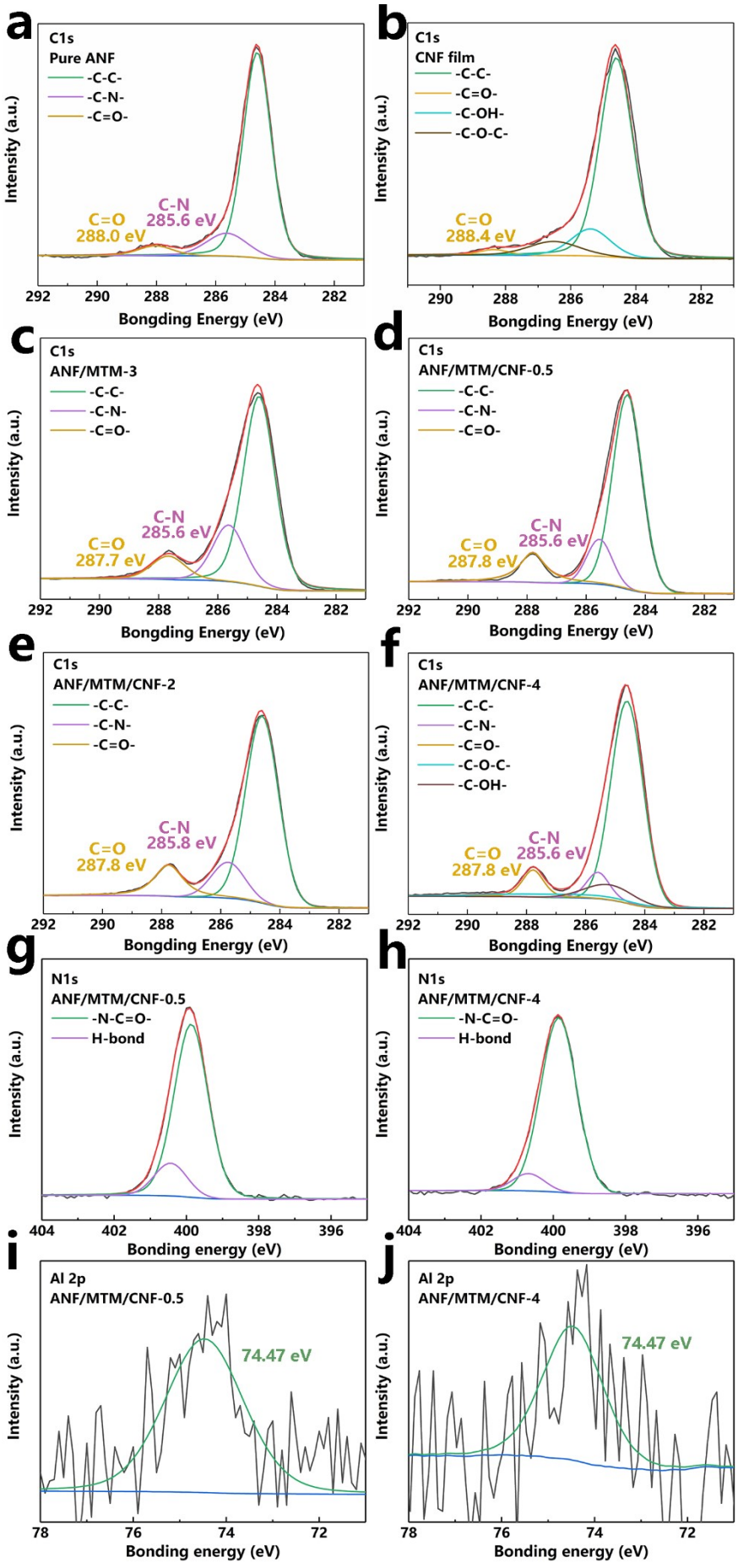
a
C1s
Pure ANF
-C-C-
-C-N-
-C=O-
C=O
288.0 eV
C-N
285.6 eV
Intensity (a.u.)
292 290 288 286 284 282
Bongding Energy (eV)
b
C1s
CNF film
-C-C-
-C=O-
-C-OH-
-C-O-C-
C=O
288.4 eV
Intensity (a.u.)
290 288 286 284 282
Bongding Energy (eV)
c
C1s
ANF/MTM-3
-C-C-
-C-N-
-C=O-
C=O
287.7 eV
C-N
285.6 eV
Intensity (a.u.)
292 290 288 286 284 282
Bongding Energy (eV)
d
C1s
ANF/MTM/CNF-0.5
-C-C-
-C-N-
-C=O-
C=O
287.8 eV
C-N
285.6 eV
Intensity (a.u.)
292 290 288 286 284 282
Bongding Energy (eV)
e
C1s
ANF/MTM/CNF-2
-C-C-
-C-N-
-C=O-
C=O
287.8 eV
C-N
285.8 eV
Intensity (a.u.)
292 290 288 286 284 282
Bongding Energy (eV)
f
C1s
ANF/MTM/CNF-4
-C-C-
-C-N-
-C=O-
-C-O-C-
-C-OH-
C=O
287.8 eV
C-N
285.6 eV
Intensity (a.u.)
292 290 288 286 284 282
Bongding Energy (eV)
g
N1s
ANF/MTM/CNF-0.5
-N-C=O-
H-bond
Intensity (a.u.)
404 402 400 398 396
Bonding energy (eV)
h
N1s
ANF/MTM/CNF-4
-N-C=O-
H-bond
Intensity (a.u.)
404 402 400 398 396
Bonding energy (eV)
i
Al 2p
ANF/MTM/CNF-0.5
74.47 eV
Intensity (a.u.)
78 76 74 72
Bonding energy (eV)
j
Al 2p
ANF/MTM/CNF-4
74.47 eV
Intensity (a.u.)
78 76 74 72
Bonding energy (eV)

Figure.S7 (a-f) XPS C_{1s} spectra of the (a) pure ANF, (b) pure CNF, (c) ANF/MTM-3, (d) ANF/MTM/CNF-0.5, (E) ANF/MTM/CNF-2, and (f) ANF/MTM/CNF-4 nanopapers. (g-h) XPS N_{1s} spectra of the (g) ANF/MTM/CNF-0.5, (h) ANF/MTM/CNF-4 nanopapers. (i-j) XPS Al_{2p} spectra of the (i) ANF/MTM/CNF-0.5, (j) ANF/MTM/CNF-4 nanopapers.

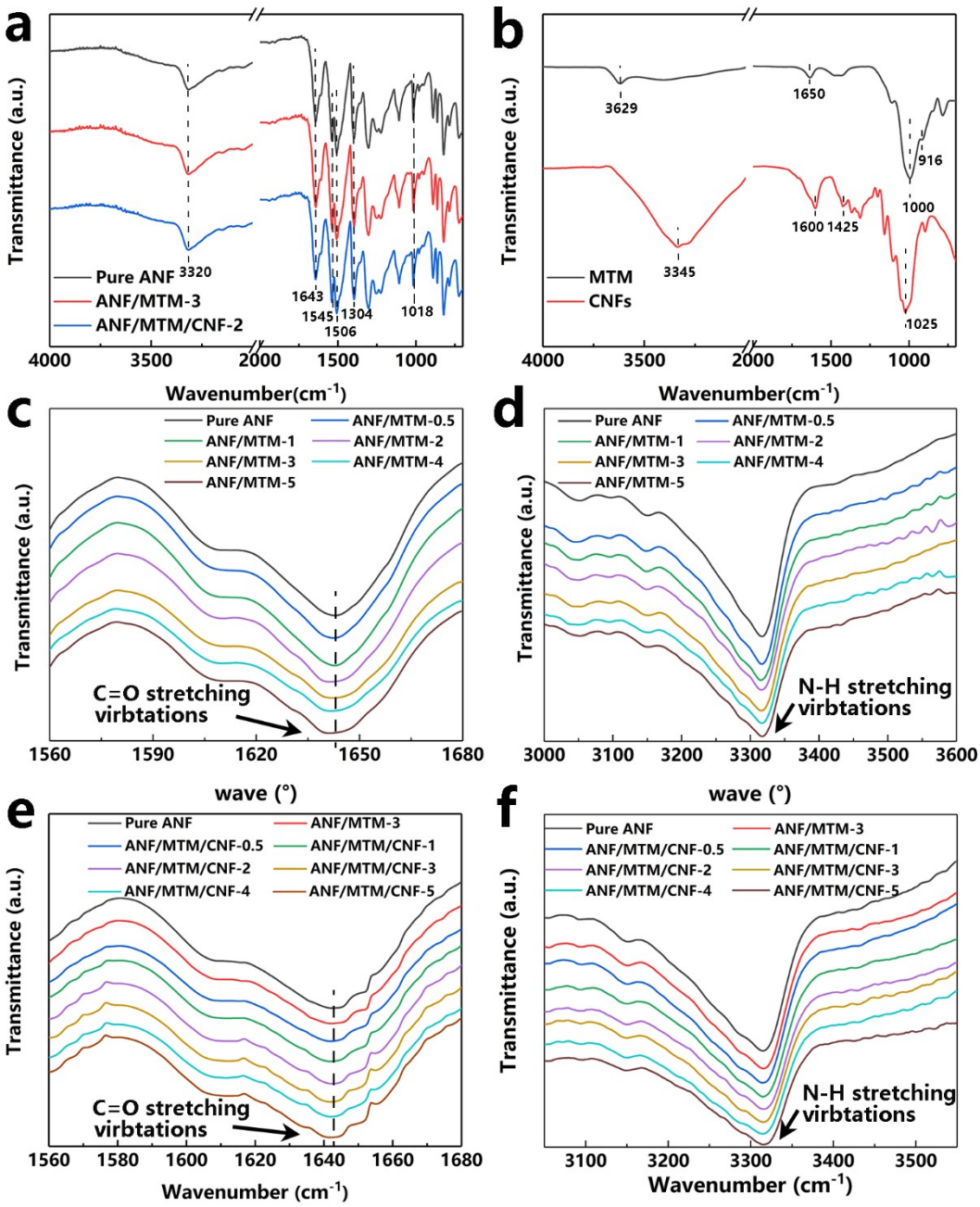

Figure.S8 (a) FTIR spectra of the pure ANF, ANF/MTM-3, and ANF/MTM/CNF-2 nanopapers. (b) FTIR spectra of the MTM nanoplates and the pure CNF nanopapers. (c) The C=O stretching vibrations and (d) the N-H stretching vibrations of FTIR spectra of the pure ANF, ANF/MTM nanopapers. (e) The C=O stretching vibrations and (f) the N-H stretching vibrations of FTIR spectra of the pure ANF, ANF/MTM-3, and ANF/MTM/CNF nanopapers.

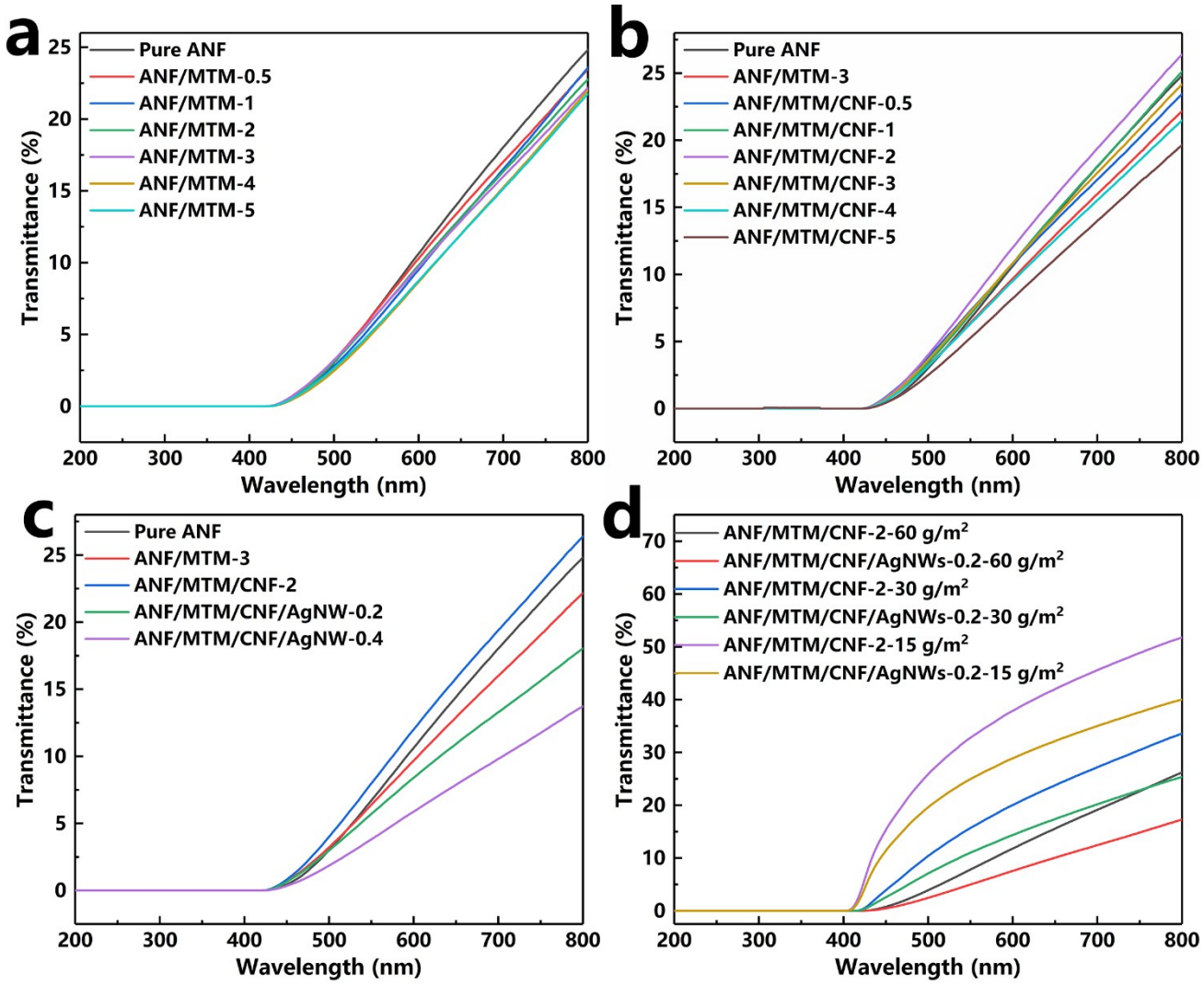

Figure.S9 UV-vis transmittance of the pure ANF, (a) ANF/MTM, (b) ANF/MTM/CNF, (c) ANF/MTM/CNF/AgNW nanopapers, and several nanopapers with different grammage.

The transparency of various nanopapers was characterized and displayed in **Fig. S9**. Achieving nanopapers with 100% transmittance is highly challenging due to the presence of inherent defects, which result in light scattering. The primary cause of light scattering is the difference between air (1.00) and the matrix in refractive index.[2] Because of the large size and high aspect ratio of ANFs, the pure ANF nanopapers had a low transparency with a value of 24.83% at 800 nm. Meanwhile, as the result of the difference in refractive index between MTM (~1.50) and ANFs (1.62~2.10),[3] the introduction of MTM nanoplates further decreased the transparency of nanopapers. While the

introduction of MTM nanoplates in ANF nanopapers reduced the overall porosity, it is important to note that the high aspect ratio of MTM nanoplates may only decrease the volume of defects rather than their actual number. Conversely, the refractive index of cellulose was also about 1.50, but the ANF/MTM/CNF-2 nanopapers had a higher transparency than the ANF/MTM-3 nanopapers, which can be attributed to the filling of interstices by CNFs within the ANF/MTM network. This filling effect reduced the number and volume of defects in the nanopapers, leading to a decrease in light scattering between air and ANFs and ultimately resulting in improved transparency.[3] Upon the introduction of AgNWs, the transparency of nanopapers decreased obviously due to the non-transparency of Ag. In general, as the result of the UV-absorbance of aramid, all nanopapers displayed a superior UV-shielding performance (≥ 99.999% absorption for ultraviolet radiation). The UV-vis transmittance of nanopapers with varying grammages was assessed, as shown in **Fig. S9d**. The ANF/MTM/CNF-2 nanopapers, with a grammage of 15 g/m^2, had a thickness of 11.0 μm and exhibited high transparency, reaching 51.79% at 800 nm. Even with the introduction of AgNWs, the nanopapers still maintained a relatively high transparency of 40.03% at 800 nm. Additionally, both the ANF/MTM/CNF-2-15 g/m^2 and ANF/MTM/CNF/AgNW-2-15 g/m^2 nanopapers demonstrated excellent UV-shielding performance, with an absorption rate of≥99.99% for ultraviolet radiation. This remarkable capability highlights their significant potential in the field of UV shielding.

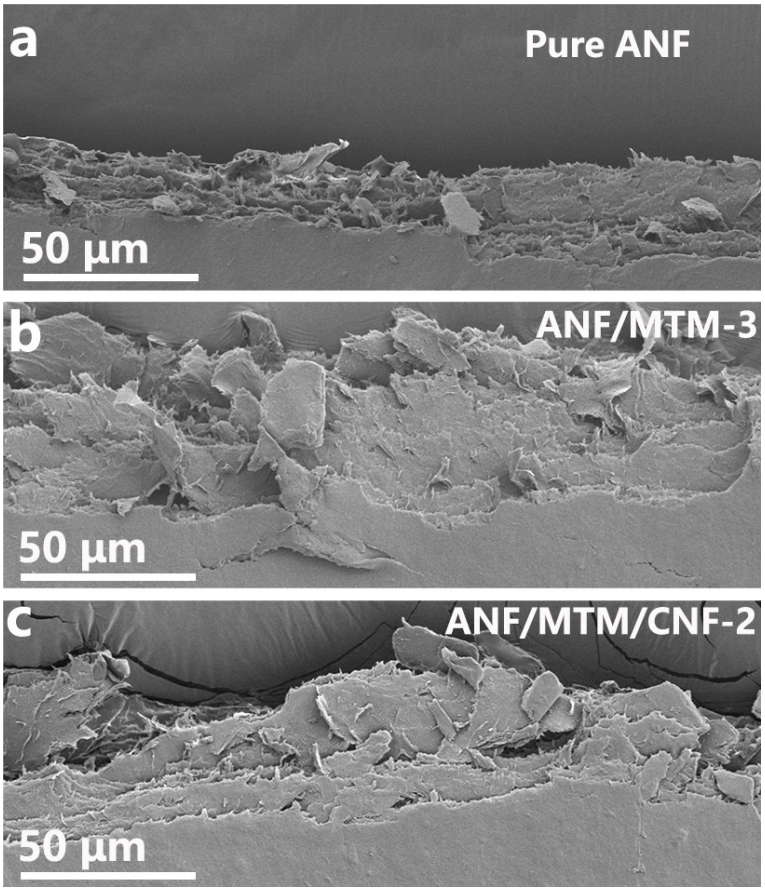

Figure.S10 The sectional images of fractured location of (a) the pure ANF, (b) ANF/MTM-3, and (c) ANF/MTM/CNF-2 nanopapers.

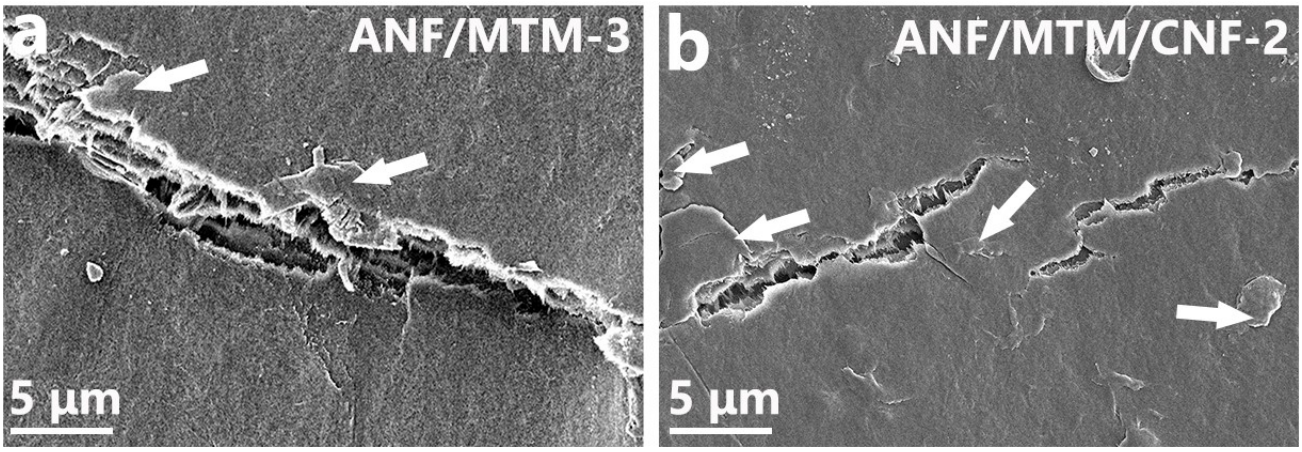

Figure.S11 The cracks on the surface of the fractured (a) ANF/MTM-3 and (b) ANF/MTM/CNF-2 nanopapers.

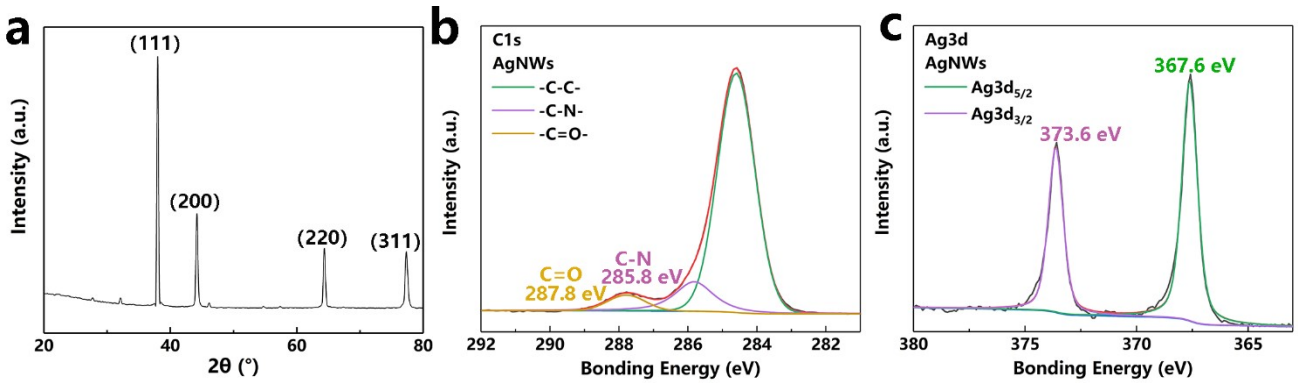

Figure.S12 (a) XRD spectra of AgNWs. XPS (b) C_{1s} and (c) Ag_{3d} spectra of AgNWs.

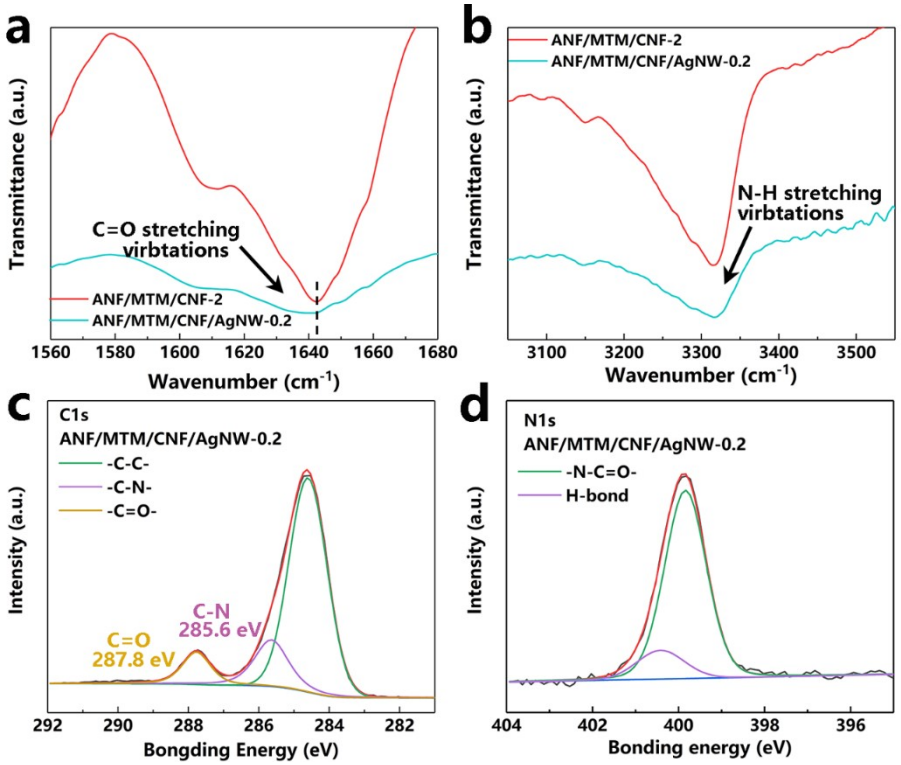

Figure.S13 (a) The C=O stretching vibrations and (b) the N-H stretching vibrations of FTIR spectra of the ANF/MTM/CNF-2 and ANF/MTM/CNF/AgNW-0.2 nanopapers. XPS (c) C_{1s} and (d) N_{1s} spectra of the ANF/MTM/CNF/AgNW-0.2 nanopaper.

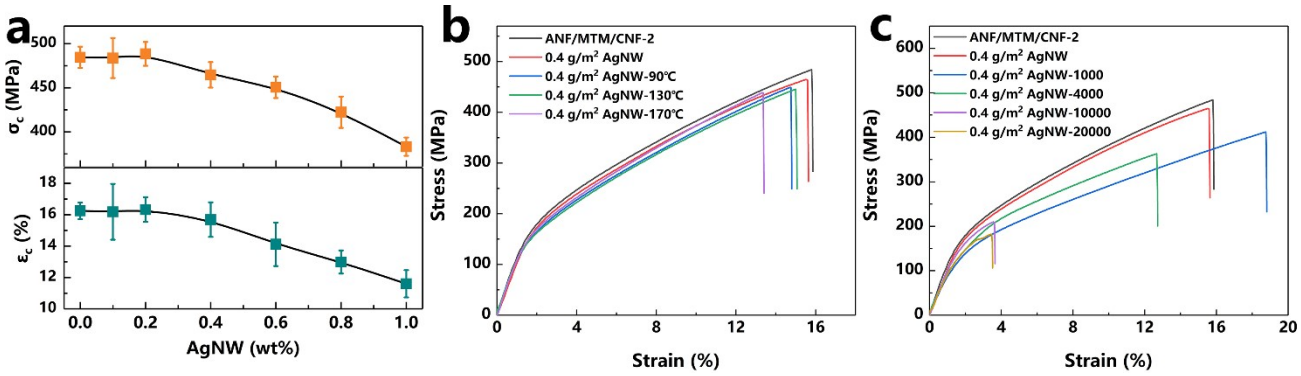

Figure.S14 (a) Tensile stress (δ_c) and elongation (ε_c) as a function of grammage of AgNW to ANF/MTM/CNF-2 nanopaper. (b) Stress-strain curves of the ANF/MTM/CNF/AgNW-0.4 nanopapers were electrical heating at 90, 130, and 170 ℃ for 1 h. (c) Stress-strain curves of the ANF/MTM/CNF/AgNW-0.4 nanopapers were folded 1000, 4000, 10000, and 20000 times.

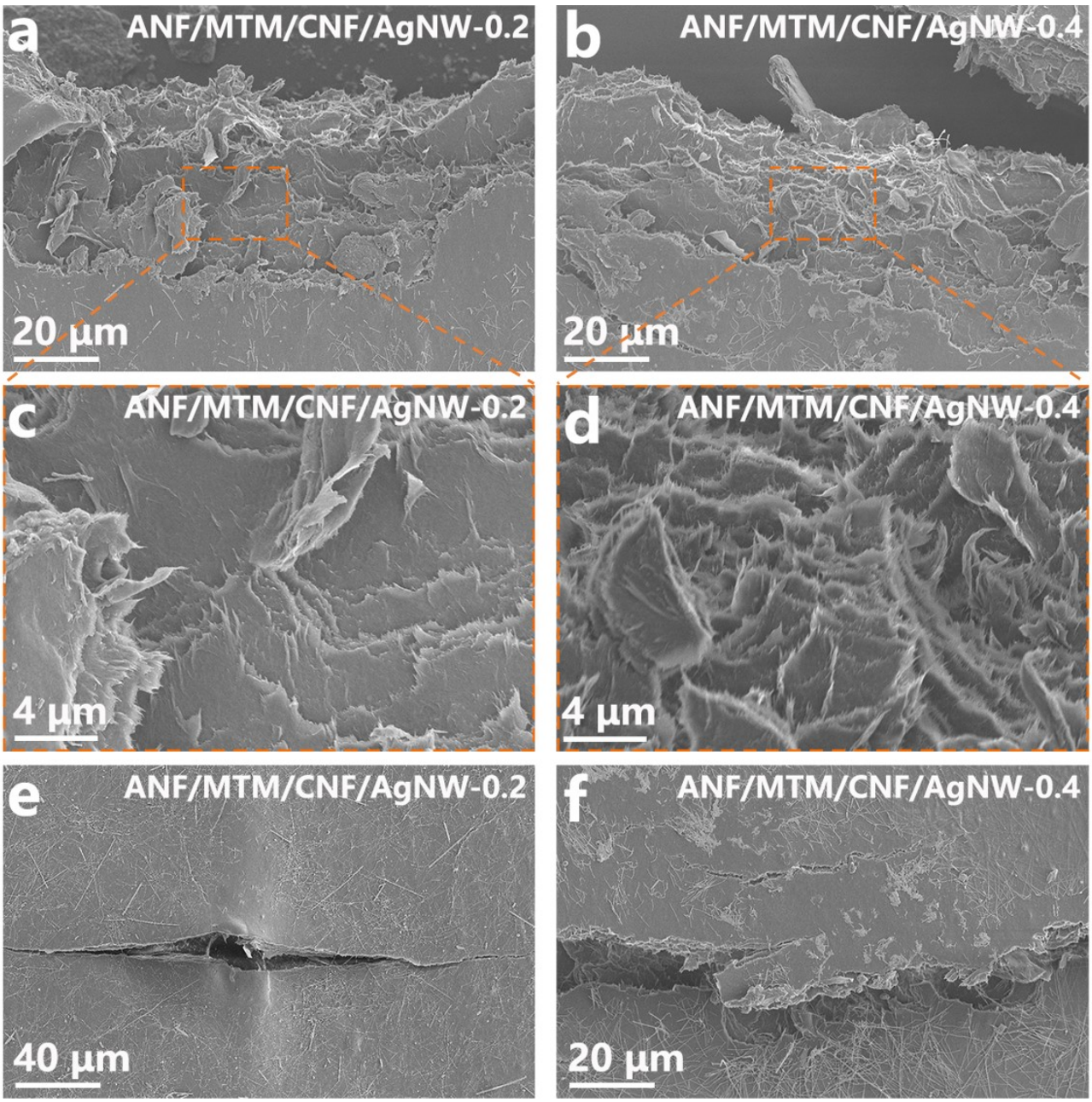

Figure.S15 (a-d) The sectional images of fractured location of (a, c) the ANF/MTM/CNF/AgNW-0.2, and (a, c) the ANF/MTM/CNF/AgNW-0.4 nanopapers. (e-f) The cracks on the surface of the fractured (e) ANF/MTM/CNF/AgNW-0.2 and (f) ANF/MTM/CNF/AgNW-0.4 nanopapers.

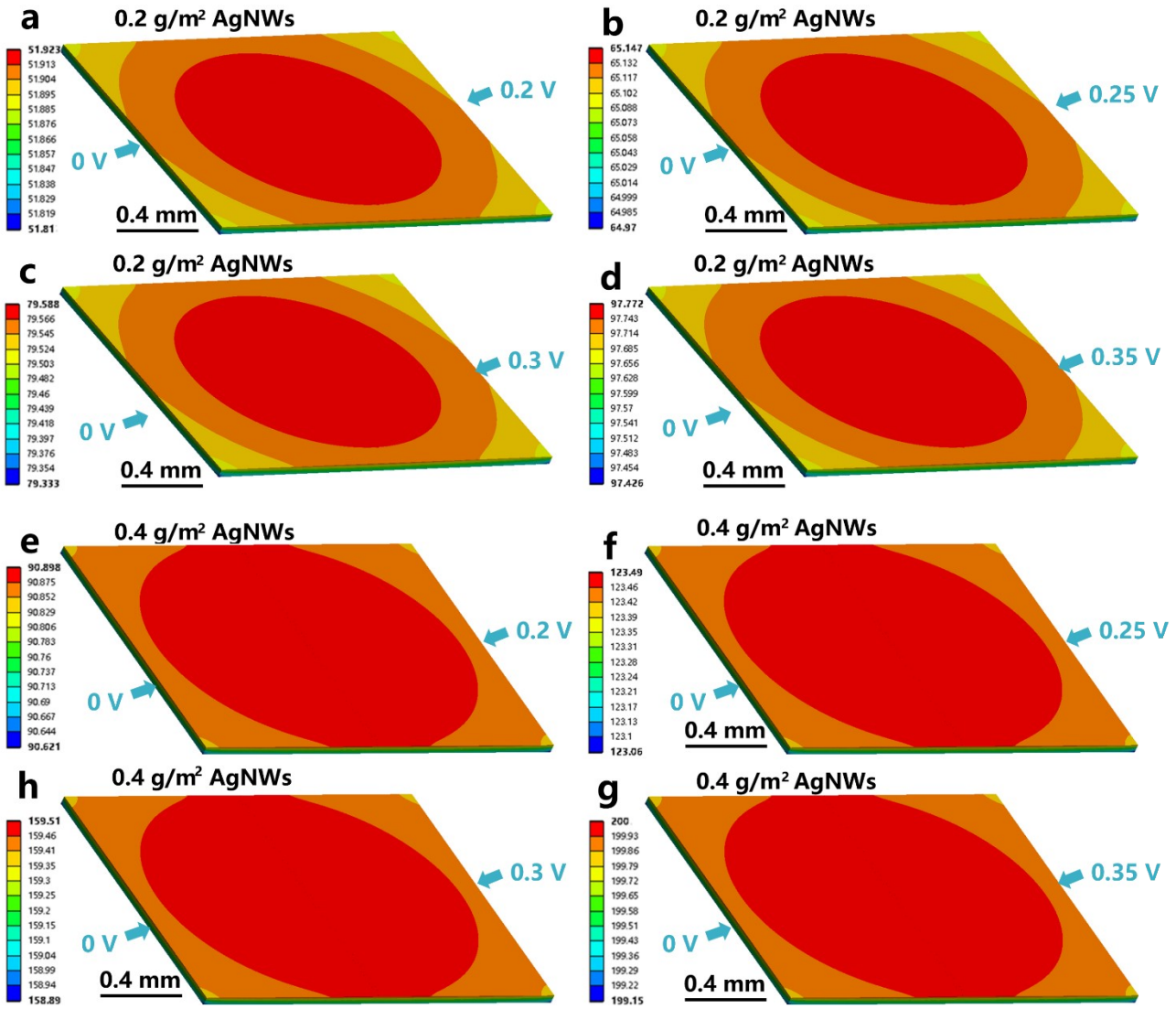

Figure.S16 Simulation of (a-d) ANF/MTM/CNF/AgNW-0.2, and (e-g) ANF/MTM/CNF/AgNW-0.4 nanopapers with size of 1.5 mm × 2.1 mm loading different voltage made by ANSYS simulation software.

To explain and intuitively understand the electrical heating mechanism of the ANF/MTM/CNF/AgNW nanopapers, ANSYS thermal-electric simulation was performed to analyze the temperature variation when different voltage was applied. As the result of the size limitations of the ANSYS thermal-electric module, it is unable to simulate the electrothermal process of excessively thin models. The dimensions of the nanopaper model were set to one-tenth of the actual experimental size for length and width, while the thickness remained the same as the actual size. In electrical heating

performance characterization, the nanopapers were cut into rectangular-shaped coupons of 15 mm × 25 mm. Silver paste was applied to both ends of the coupons, with a width of 2 mm on each side. In other word, the actual electrical heating area of the nanopapers is 15 mm × 21 mm. Therefore, in the simulation, the length and width of the nanopaper models were set as 2.1 mm and 1.5 mm, respectively, and the voltage applied at their two ends was also scaled down by a factor of one-tenth of the actual value. Prior to the simulation, the specific resistance of the AgNW layers in the ANF/MTM/CNF/AgNW-0.2 and ANF/MTM/CNF/AgNW-0.4 nanopapers was measured using a four-point probe tester. The thickness of the AgNW layers was estimated by subtracting the thickness of the ANF/MTM/CNF-2 nanopaper from that of the ANF/MTM/CNF/AgNW nanopaper. Upon testing, the resistivity of the AgNW layers in the ANF/MTM/CNF/AgNW-0.2 and ANF/MTM/CNF/AgNW-0.4 nanopapers were 5.908 ± 0.850 Ω·μm and 3.828 ± 0.102 Ω·μm, respectively. Other simulation parameters were all provided in **Table S6**. As shown in **Fig. S16**, the ANF/MTM/CNF/AgNW nanopapers were applied with voltage of 0.2, 0.25, 0.3, and 0.35 V. Upon the application of voltage, the temperature of the ANF/MTM/CNF/AgNW-0.2 nanopapers reached 51.9, 65.1, 79.6, and 97.8 ℃, respectively, demonstrating excellent agreement with the experimental results showing temperatures of 52.2, 67.5, 83.3, and 99.5 ℃. For the ANF/MTM/CNF/AgNW-0.4 nanopaper, in the simulation, with voltage of 0.2, 0.25, 0.3, and 0.35 V, its temperature was 90.9, 123.5, 159.5, and 200.0 ℃, which also were in good agreement with the experimental results with temperature of 97.1, 125.2, 162.0, and 192.8℃. The simulation results indicate that the electrical heating performance of the nanopaper is directly correlated to the resistivity and thickness of its conductive layer. Lower resistivity and greater thickness of the conductive layer result in higher electrical heating temperatures under the same applied voltage. Furthermore, during the simulation,

adjusting the time parameter has no effect on the electrical heating temperature. This indicates that for the nanopaper reaching a steady-state temperature, extending the duration does not cause any change in its electrical heating temperature unless there are changes in its own resistance.

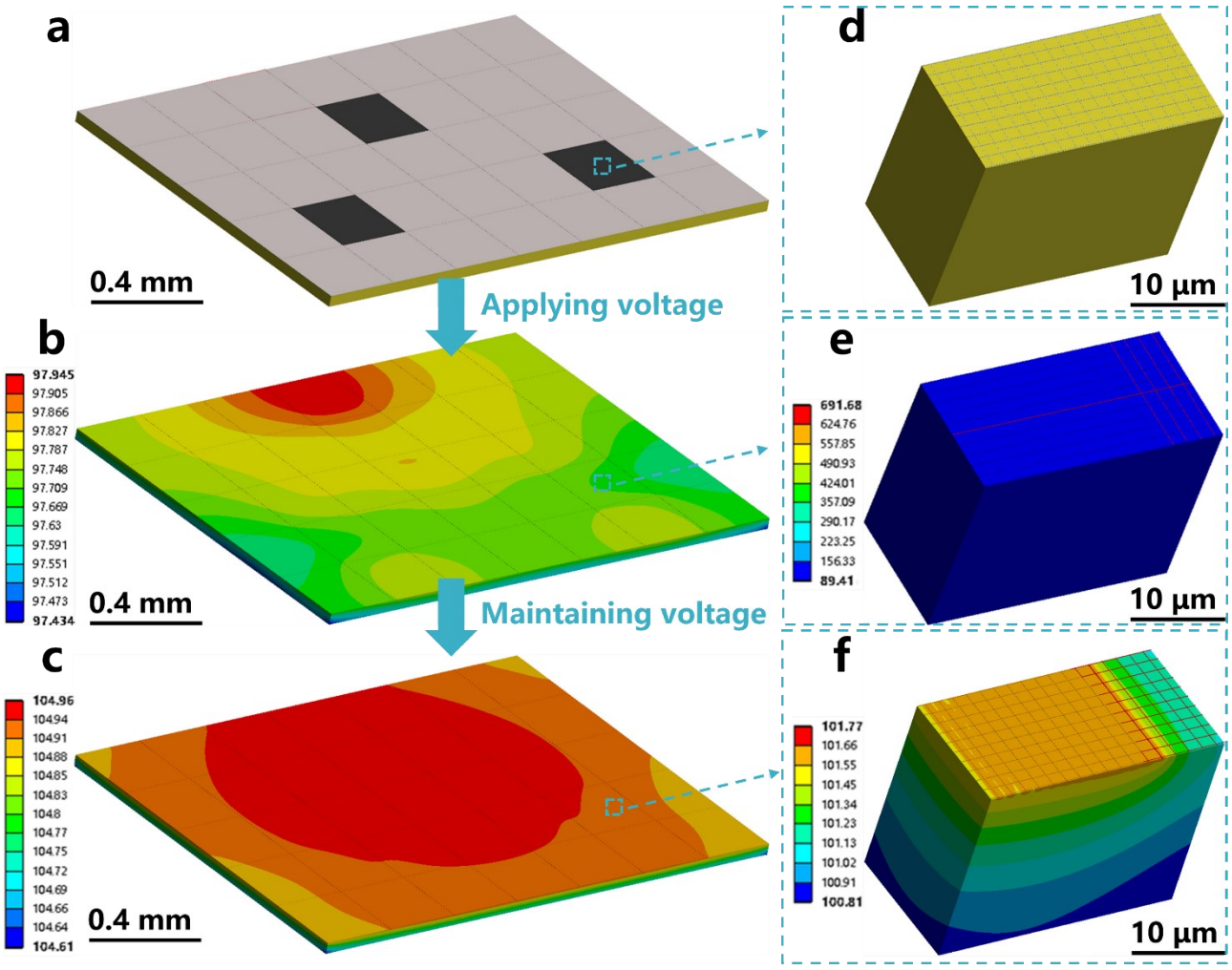

Figure.S17 Investigation of the mechanism for surface temperature increase during long-term electrical heating test made by ANSYS simulation software.

ANSYS thermal-electric simulation was conducted in an attempt to provide a theoretical explanation for the phenomenon of temperature increase observed in the steady-state of the ANF/MTM/CNF/AgNW nanopaper during the electrical heating process (**Fig. 7f** and **g**). In electrical heating nanopapers, as the result of the excess rigidity of AgNWs, achieving perfect and consistent contact between AgNWs and between AgNWs and the substrate throughout the nanopaper is challenging. Poor contact between the AgNWs can result in an increased resistance in specific regions.

Additionally, inadequate heat dissipation can occur in the regions with poor contact between AgNWs and between AgNWs and the substrate, leading to elevated temperatures in the affected AgNWs. As shown in **Figure. S17,** during simulation, two models were constructed. For the model in **Figure. S17a**, its dimensions were consistent with the model depicted in **Figure S16a**. In the model, the AgNW layer was assigned two different colors, where the black regions had a resistivity five times higher than the gray regions, indicating areas of poor contact between the AgNWs. The substrate model in **Figure. S17b** had a length of 30 μm, a width of 15 μm, and a thickness of 21.8 μm. The AgNW model was simplified as rectangular prisms with uniform width and height of 80 nm, arranged in a perpendicular cross pattern on the substrate model. The models in **Figure. S17b**, **d**, and **f** represented the microstructural changes during electrical heating for the nanopapers. As shown in **Figure. S17c**, upon applying voltage, the temperature of the model with three areas of high resistance reached around 97.7℃. In the model depicted in **Figure S17d**, specific areas of contact between AgNWs and between AgNWs and the substrate were intentionally disabled to represent regions of poor contact. Upon applying voltage, the temperature of AgNWs in these regions reached 691.7℃, while the temperature of the substrate remained at 89.4℃. In the model shown in **Figure. S17f**, two previously disabled contacts between AgNWs were reestablished to simulate the thermal welding process, resulting in a uniform temperature distribution throughout the model. Correspondingly, the resistivity of the three black regions in the model in **Figure. S17g** was reduced to 1.5 times that of the gray regions, representing a decrease in resistance due to thermal welding. As a result, the temperature of the model increased to approximately 104.9℃. In general, poor contact could occur at various locations within the electrical heating nanopaper. However, once the AgNWs with poor contact undergone thermal welding due to localized high temperatures, new conductive networks were formed, along with new

heat transfer paths. This enabled efficient heat transfer to the substrate, ultimately resulting in a fully stable conductive and thermal network throughout the electrical heating nanopaper. Consequently, as thermal welding established new conductive pathways, the resistance in the affected regions decreased, ultimately leading to an increase in the steady-state temperature of the electrical heating nanopaper. Certainly, if there were regions with insufficient distribution of AgNWs, the local high temperatures resulting from poor contact may lead to complete melting of the AgNWs, thereby completely disrupting the conductive pathway in that area. As a result, the increased local resistance could cause a decrease in the steady-state temperature of the electrical heating nanopaper.

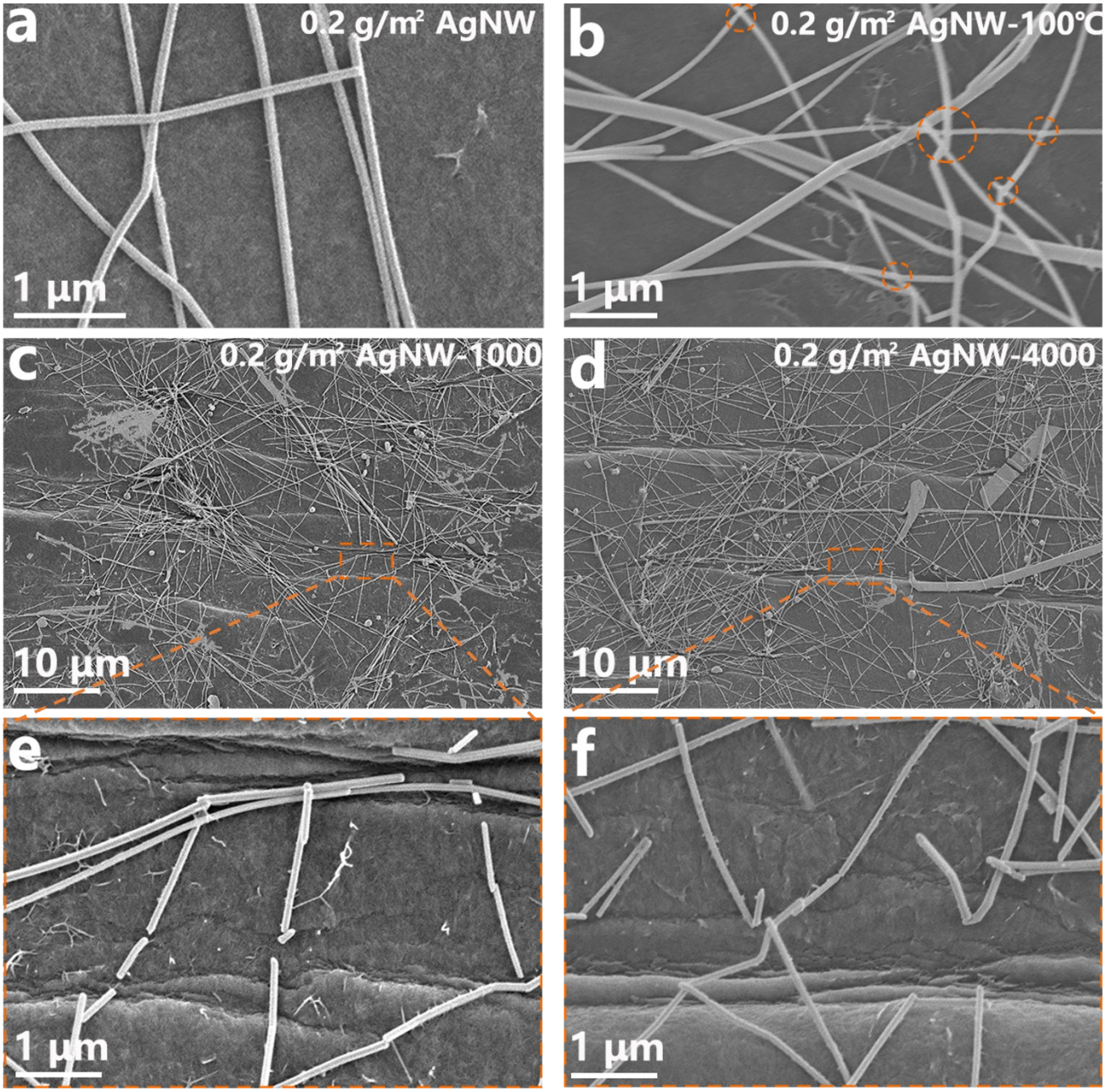

Figure.S18 The surface images of the original ANF/MTM/CNF/AgNW-0.2 nanopaper (a) and the nanopapers were supplied with a constant voltage of 3.5 V for 1h (b), and were folded (c, d) 1000 and (e, f) 4000 times.

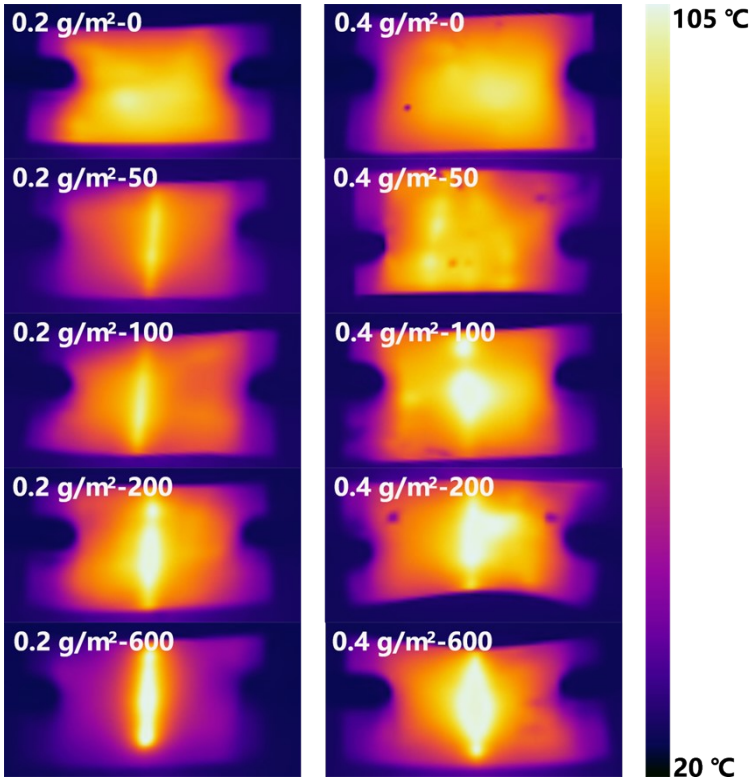

Figure.S19 Infrared thermal images of the ANF/MTM/CNF/AgNW-0.2 and ANF/MTM/CNF/AgNW-0.4 nanopapers, which were folded 0, 50, 100, 200, 600 times, under supplied voltages.

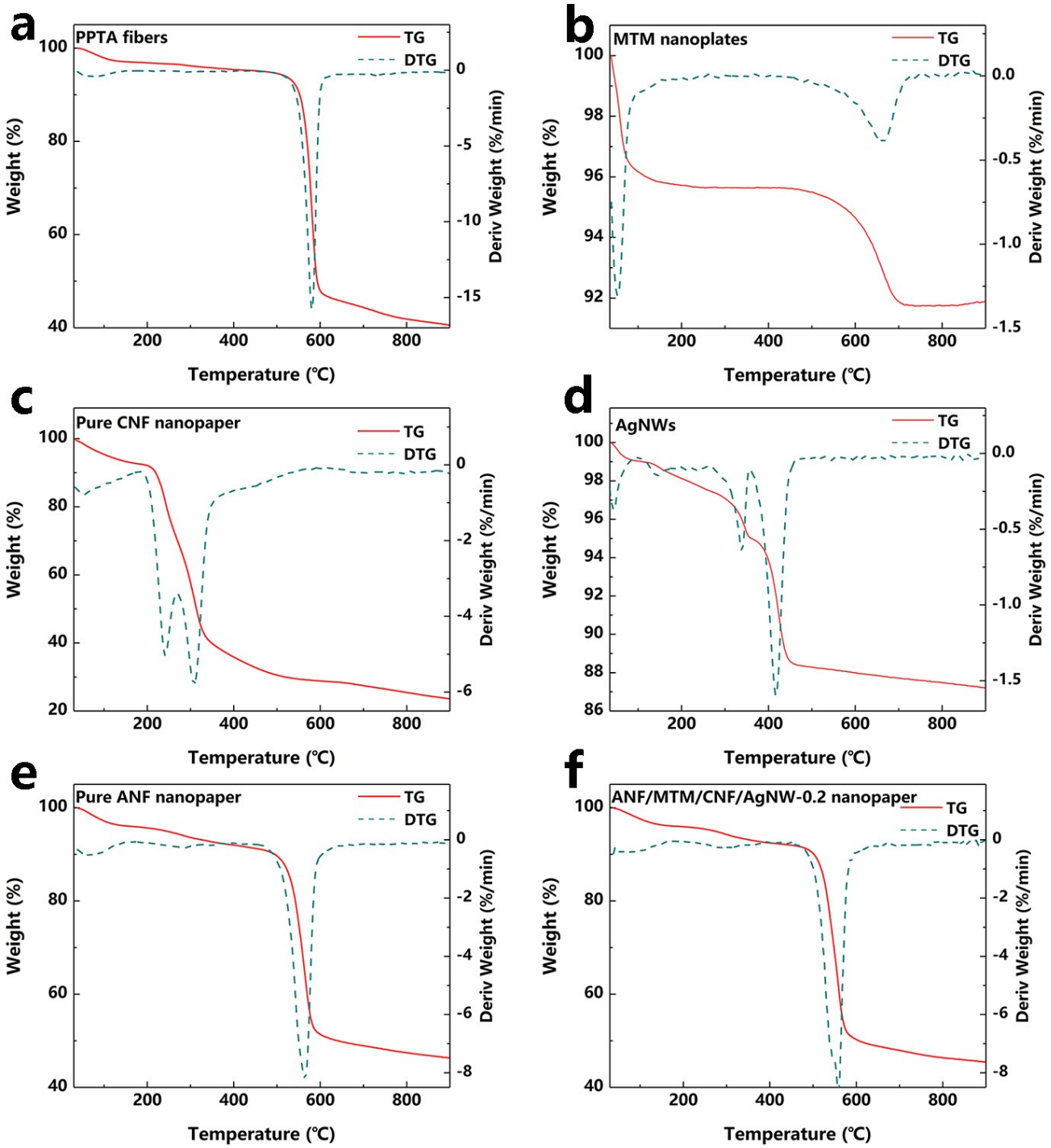

Figure.S20 TG and DTG curves of (a) PPTA fibers, (b) MTM nanoplates, (c) pure CNF nanopapers, (d) AgNWs, (e) pure ANF nanopapers, and (f) ANF/MTM/CNF/AgNW-0.2 nanopapers.

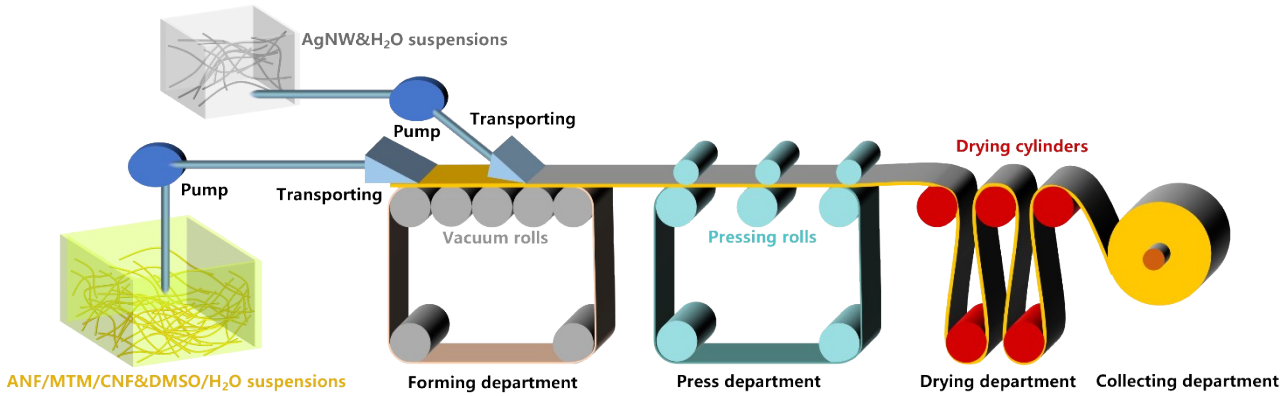

Figure.S21 Schematic diagram illustrating the modern papermaking technique for the large-scale preparation of ANF/MTM/CNF/AgNW nanopapers.

Table S1. The retention rate of ANFs, MTM nanoplates, and CNFs after vacuum-assisted filtration.

Sample	ANFs	MTM nanoplates	CNFs
Retention rate	98.46 (0.38)	97.86 (2.64)	98.01 (1.72)

Table S2. Mechanical properties of the pure ANF, ANF/MTM0, ANF/MTM, and ANF/LN nanopapers

Sample	Strength（MPa）	Mdulus（GPa）	Strain（%）	Toughness（MJ/m^3）	Thickness (μm)
Pure ANF	222.10 (13.29)	5.43 (0.11)	13.99 (0.38)	19.85 (1.44)	48.77 (0.39)
ANF/MTM0-0.25	283.40 (5.70)	5.71 (0.44)	15.33 (1.54)	27.07 (2.43)	47.77 (0.29)
ANF/MTM0-0.5	313.04 (19.76)	6.16 (0.35)	16.45 (1.87)	37.63 (4.31)	47.29 (1.02)
ANF/MTM0-1	368.88 (13.57)	7.20 (0.32)	19.75 (1.67)	45.62 (2.16)	45.79 (0.16)
ANF/MTM0-2	393.65 (15.67)	7.03 (0.28)	19.81 (1.67)	48.82 (1.15)	43.67 (0.56)
ANF/MTM0-3	399.00 (11.18)	6.81 (0.47)	21.41 (1.85)	53.76 (4.34)	44.45 (0.65)
ANF/MTM0-4	375.36 (10.52)	6.73 (0.23)	20.47 (1.63)	52.20 (1.94)	45.15 (0.63)
ANF/MTM0-5	325.31 (10.81)	6.48 (0.14)	16.82 (1.26)	34.87 (2.48)	45.51 (0.49)
ANF/MTM-0.25	305.27 (13.99)	6.02 (0.18)	17.90 (1.73)	37.52 (3.47)	48.38 (0.84)
ANF/MTM-0.5	342.41 (14.20)	6.52 (0.37)	20.24 (1.41)	47.20 (4.81)	47.64 (0.52)
ANF/MTM-1	365.26 (12.61)	7.13 (0.16)	19.51 (1.18)	50.29 (5.37)	47.29 (0.72)
ANF/MTM-2	377.41 (11.96)	7.80 (0.24)	18.78 (1.90)	51.36 (3.32)	46.40 (0.86)
ANF/MTM-3	412.18 (18.99)	8.28 (0.24)	18.25 (1.78)	54.75 (4.29)	45.60 (0.75)
ANF/MTM-4	408.12 (9.96)	8.42 (0.30)	18.08 (1.39)	48.60 (3.12)	44.97 (0.37)
ANF/MTM-5	331.29 (27.92)	7.88 (0.33)	14.63 (3.07)	34.23 (8.15)	44.68 (0.53)
ANF/LN-0.25	314.75 (20.72)	6.10 (0.27)	17.35 (1.29)	31.47 (6.45)	46.19 (0.23)
ANF/LN-0.5	367.79 (15.23)	6.89 (0.34)	18.50 (1.53)	48.70 (3.41)	45.72 (0.61)
ANF/LN-1	386.10 (13.19)	7.28 (2.77)	20.76 (1.47)	53.02 (2.50)	44.35 (0.49)
ANF/LN-2	394.64 (12.07)	7.52 (0.25)	20.14 (1.41)	51.92 (1.88)	43.90 (0.78)
ANF/LN-3	401.39 (15.31)	7.94 (0.35)	17.27 (1.81)	47.74 (3.44)	42.35 (0.57)
ANF/LN-4	333.63 (16.84)	6.99 (0.25)	16.19 (1.67)	37.30 (5.00)	43.27 (0.60)
ANF/LN-5	289.90 (17.91)	5.88 (0.43)	14.27 (3.07)	27.59 (2.39)	46.32 (0.55)

Table S3. Mechanical properties of the pure ANF, ANF/MTM-3, ANF/MTM/CNF, and ANF/MTM/CNF/AgNW nanopapers

Sample	Strength（MPa）	Mdulus（GPa）	Strain（%）	Toughness（MJ/m^3）	Thickness (μm)
Pure ANF	222.10 (13.29)	5.43 (0.11)	13.99 (0.38)	19.85 (1.44)	48.77 (0.39)
ANF/MTM-3	412.18 (18.99)	8.28 (0.24)	18.25 (1.78)	54.75 (4.29)	45.60 (0.75)
ANF/MTM/CNF-0.5	431.13 (31.98)	10.56 (0.18)	17.13 (1.32)	52.00 (7.28)	45.53 (0.69)
ANF/MTM/CNF-1	465.31 (16.39)	10.58 (0.29)	16.87 (1.09)	51.92 (4.60)	44.59 (0.20)
ANF/MTM/CNF-2	484.58 (12.03)	11.36 (0.42)	16.25 (0.53)	53.70 (4.49)	43.63 (0.26)
ANF/MTM/CNF-3	466.78 (13.33)	11.88 (0.77)	15.24 (1.34)	47.68 (2.63)	44.45 (0.75)
ANF/MTM/CNF-4	423.58 (10.03)	10.99 (0.33)	14.26 (1.18)	38.40 (2.23)	45.91 (0.30)
ANF/MTM/CNF-5	376.28 (9.22)	10.65 (0.39)	13.74 (0.78)	34.37 (1.74)	48.35 (0.38)
ANF/MTM/CNF/AgNW-0.1	483.71 (22.71)	11.76 (0.55)	16.19 (1.78)	52.05 (3.40)	43.86 (0.58)
ANF/MTM/CNF/AgNW-0.2	488.48 (13.54)	11.79 (0.39)	16.33 (0.79)	52.74 (2.76)	44.09 (0.51)
ANF/MTM/CNF/AgNW-0.4	464.70 (14.46)	11.89(0.74)	15.69 (1.10)	48.53 (1.76)	44.45 (0.65)
ANF/MTM/CNF/AgNW-0.6	450.59 (12.24)	12.20 (0.44)	14.12 (1.39)	42.39 (2.51)	44.73 (0.33)
ANF/MTM/CNF/AgNW-0.8	422.36 (17.78)	12.04 (0.40)	12.99 (0.74)	38.36 (4.98)	45.06 (0.71)
ANF/MTM/CNF/AgNW-1.0	383.23 (10.35)	11.66 (0.75)	11.60 (0.87)	30.08 (3.85)	45.28 (0.69)

Table S4. Reference details in Fig. 6d.

Matrix	Reinforcement	Tensile strength (MPa)		Strain-to-failure (%)		Reference
		Before	After	Before	After	
Polypropylene	CNT	68.3	79.6	9.6	7.8	4
Polypropylene	Graphene	66.5	70.1	102.0	38.0	5
Polypropylene	L-CNFs	30.6	38.3	3.3	2.8	6
PLA	Ramie fiber	45.2	66.8	1.2	4.8	7
PLA	Cellulose Fibers	60.8	94.6	3.0	1.9	8
PLA	CNCs	52.1	56.3	32.1	5.6	9
PMMA	Chitin nanofibers	29.8	37.7	3.6	5.6	10
PMMA	Delignified wood	44.1	90.1	6.6	3.5	11
PMMA	CNFs	53.2	56.6	2.7	2.8	12
PVA	L-CNFs	43.6	72.8	420.0	445.0	13
PVA	Clay	145.0	220.0	30.0	1.4	14
PVA	GO	87.0	115.0	120.0	195.0	15
Mg alloys		95.0 - 285.0		2.0 - 16.5		16
Al - Li alloys		295.0 - 550.0		10.0 - 15.6		17
Fe-Mn-Al-C		808.0 - 1251.0		1.1 - 65.6		18
High-specific-strength steel		1340.0 - 1520.0		18.0 - 31.0		19
Fiberglass		2000.0 - 4570.0		2.5 - 2.8		20
Kevlar fiber		2920 - 3600		2.4 – 3.6		21
UHMWPE		3360 - 5170		3.2 – 4.7		22
ANFs	MTM	222.1	412.2	14.0	18.3	This work
ANFs	MTM/CNF	222.1	484.6	14.0	16.3	
ANFs	MTM/CNF/AgNW	222.1	488.5	14.0	16.3	

Table S5. Reference details in Figure 6f.

Sample	Tensile strength (MPa)	Toughness (MJ/m3)	Reference
ANFs/MXene/AgNW	198.8	21.9	23
Anisotropic ANFs/PVA	296.0	10.0	24
ANFs/MXene	305.5	5.3	25
ANFs/AgNW	285.7	19.0	26
Anisotropic ANFs/GO	616.3	16.5	27
ANFs/GnP	437.0	23.9	28
Anisotropic ANFs/clay	496.6	13.6	29
ANFs/GO	377.0	8.0	30
ANFs/BNNS	215.0	9.5	31
ANFs/CNT	361.0	2.3	32
ANFs/PVA	279.5	35.7	33
ANFs/PDA	227.0	32.0	34
ANFs/graphene fluoride	188.0	107.0	35
This work	412.2	54.8	-
	484.6	53.7	-
	488.5	52.7	-

Table S6. ANSYS thermal-electric simulation parameters of ANF/MTM/CNF/AgNW nanopaper

Parameters/Sample	ANF/MTM/CNF/AgNW-0.2	ANF/MTM/CNF/AgNW-0.4
Ambient temperature	22 ℃	
Voltage type	DC. voltage	
Mesh quality	Tetrahedron /Quadratic	
ANF/MTM/CNF layer thickness	43.63 μm	
AgNW layer thickness	0.46 μm	0.82 μm
ANF/MTM/CNF layer thermal conductivity	0.23 W/(m·K)	
AgNW layer thermal conductivity	429 W/(m·K)	
AgNW layer resistivity	5.908 Ω·μm	3.828 Ω·μm

Table S7. The resistance of ANF/MTM/CNF/AgNW-0.2 and ANF/MTM/CNF/AgNW-0.4 electrical heaters with size of 15 mm × 25 mm after several folding cycles.

Folding cycles	ANF/MTM/CNF/AgNW-0.2		ANF/MTM/CNF/AgNW-0.4	
(times)	Resistence (Ω)	R/R_0	Resistence (Ω)	R/R_0
0	17.63 (0.91)	1.00	6.83 (0.22)	1.00
50	21.02 (2.57)	1.19	7.64 (0.19)	1.12
100	22.95 (1.19)	1.30	8.06 (0.78)	1.18
200	24.38 (0.39)	1.38	8.20 (0.21)	1.20
600	29.63 (0.84)	1.68	8.26 (0.39)	1.21
1000	44.29 (0.51)	2.40	8.47 (0.16)	1.24
4000	144.37 (17.67)	8.19	18.24 (0.28)	2.67
10000	383.23 (91.25)	21.74	56.67 (10.60)	8.30

Table S8. Thermal property parameters of PPTA fibers and various nanopapers

Sample	T_{onset} (℃)	T_5 (℃)	T_{30} (℃)	T_{HRI} (℃)
PPTA fiber	560.63	446.83	577.63	257.40
MTM nanoplates	580.69	572.09	-	-
Pure CNF	219.24	107.24	269.84	100.35
AgNWs	322.92	360.92	-	-
Pure ANF	530.96	242.56	557.16	211.35
ANF/MTM-3	536.79	289.19	563.99	222.49
ANF/MTM/CNF-2	522.71	255.51	549.11	211.52
ANF/MTM/CNF/AgNW-0.2	521.24	271.44	548.24	214.38
ANF/MTM/CNF/AgNW-0.4	521.17	277.77	550.17	216.19

Note: $T_{HRI} = 0.49 \times [T_5 + 0.6 \times (T_{30} - T_5)]$; T_5 and T_{30} are the corresponding decomposition temperature of 5% and 30% weight loss, respectively.[36]

Table S9. The contents of the various solid component in the ANF/MTM nanopapers obtained by TGA.

Sample	ANFs (wt%)	MTM nanoplates (wt%)
ANF/MTM-0.25	99.73 (0.14)	0.27 (0.14)
ANF/MTM-0.5	99.51 (0.11)	0.49 (0.11)
ANF/MTM-1	98.99 (0.31)	1.01 (0.31)
ANF/MTM-2	97.93 (0.59)	2.07 (0.59)
ANF/MTM-3	97.03 (0.49)	2.97 (0.49)
ANF/MTM-4	95.94 (0.32)	4.06 (0.32)
ANF/MTM-5	95.03 (0.90)	4.97 (0.90)

References

1. X. Li, A. Liu, R. Ye, Y. Wang and W. Wang, *Food Hydrocolloids*, 2015, **44**, 390-398.
2. Z. Fang, H. Zhu, W. Bao, C. Preston, Z. Liu, J. Dai, Y. Li and L. Hu, *Energy Environ. Sci.*, 2014, **7**, 3313-3319.
3. F. Hu, J. Zeng, J. Li, B. Wang, Z. Cheng, T. Wang and K. Chen, *ACS Appl Mater Interfaces*, 2022, **14**, 14640-14653.
4. Y.-M. Baek, P.-S. Shin, J.-H. Kim, H.-S. Park, K. L. DeVries and J.-M. Park, *Polymer Testing*, 2020, **81**.
5. S.-H. Yoon and H.-T. Jung, *RSC Adv.*, 2017, **7**, 45902-45910.
6. Y. Peng, S. S. Nair, H. Chen, N. Yan and J. Cao, *ACS Sustainable Chemistry & Engineering*, 2018, **6**, 11078-11086.
7. T. Yu, J. Ren, S. Li, H. Yuan and Y. Li, *Composites Part A: Applied Science and Manufacturing*, 2010, **41**, 499-505.
8. O. Oguz, K. Bilge, E. Simsek, M. K. Citak, A. A. Wis, G. Ozkoc and Y. Z. Menceloglu, *Industrial & Engineering Chemistry Research*, 2017, **56**, 8568-8579.
9. L. Zhou, H. He, M.-c. Li, S. Huang, C. Mei and Q. Wu, *Industrial Crops and Products*, 2018, **112**, 449-459.
10. F. A. Yihun, S. Ifuku, H. Saimoto, H. Izawa and M. Morimoto, *Polymer*, 2020, **197**.
11. Y. Li, Q. Fu, S. Yu, M. Yan and L. Berglund, *Biomacromolecules*, 2016, **17**, 1358-1364.
12. H. Dong, Y. R. Sliozberg, J. F. Snyder, J. Steele, T. L. Chantawansri, J. A. Orlicki, S. D. Walck, R. S. Reiner and A. W. Rudie, *ACS Appl Mater Interfaces*, 2015, **7**, 25464-25472.
13. E. Espinosa, I. Bascon-Villegas, A. Rosal, F. Perez-Rodriguez, G. Chinga-Carrasco and A. Rodriguez, *Int J Biol Macromol*, 2019, **141**, 197-206.
14. M. Morits, T. Verho, J. Sorvari, V. Liljeström, M. A. Kostiainen, A. H. Gröschel and O. Ikkala, *Advanced Functional Materials*, 2017, **27**.
15. S. Liu, J. Liu, Z. Xu, Y. Liu, P. Li, F. Guo, F. Wang, Y. Liu, M. Yang, W. Gao and C. Gao, *ACS Nano*, 2018, **12**, 11236-11243.
16. J. Xie, J. Zhang, Z. You, S. Liu, K. Guan, R. Wu, J. Wang and J. Feng, *Journal of Magnesium and Alloys*, 2021, **9**, 41-56.
17. A. Abd El-Aty, Y. Xu, X. Guo, S. H. Zhang, Y. Ma and D. Chen, *J Adv Res*, 2018, **10**, 49-67.
18. Y. Sutou, N. Kamiya, R. Umino, I. Ohnuma and K. Ishida, *Isij International*, 2010, **50**, 893-899.
19. F. J. Gil, J. M. Manero, M. P. Ginebra and J. A. Planell, *Materials Science and Engineering: A*, 2003, **349**, 150-155.
20. X. Li, L. G. Tabil and S. Panigrahi, *Journal of Polymers and the Environment*, 2007, **15**, 25-33.
21. N. Mittal, F. Ansari, V. K. Gowda, C. Brouzet, P. Chen, P. T. Larsson, S. V. Roth, F. Lundell, L. Wagberg, N. A. Kotov and L. D. Soderberg, *ACS Nano*, 2018, **12**, 6378-6388.
22. J. Penning, A. De Vries, J. V. d. Ven, A. Pinnings and H. J. P. m. A. Hoogstraten, 1994, **69**, 267-284.
23. J. Wang, X. Ma, J. Zhou, F. Du and C. Teng, *ACS Nano*, 2022, DOI: 10.1021/acsnano.2c01323.
24. D. Lee, J. Cho, J. G. Son and B. Yeom, *Composites Part B: Engineering*, 2022, **229**.
25. C. Lei, Y. Zhang, D. Liu, K. Wu and Q. Fu, *ACS Appl Mater Interfaces*, 2020, **12**, 26485-26495.
26. Z. Ma, S. Kang, J. Ma, L. Shao, A. Wei, C. Liang, J. Gu, B. Yang, D. Dong, L. Wei and Z. Ji, *ACS Nano*, 2019, **13**, 7578-7590.
27. P. Xia, H. Li, Y. Wang and J. Wang, *Applied Surface Science*, 2021, **545**.
28. M. C. Vu, P. J. Park, S.-R. Bae, S. Y. Kim, Y.-M. Kang, W. K. Choi, M. A. Islam, J. C. Won, M. Park and S.-R. Kim, *Journal of Materials Chemistry A*, 2021, **9**, 8527-8540.
29. H. Li, C. Teng, J. Zhao and J. Wang, *Composites Science and Technology*, 2021, **201**.
30. F. Wang, Y. Wu and Y. Huang, *Composites Part A: Applied Science and Manufacturing*, 2018, **110**, 126-132.
31. K. Wu, J. Wang, D. Liu, C. Lei, D. Liu, W. Lei and Q. Fu, *Adv Mater*, 2020, **32**, e1906939.

32. J. Zhu, W. Cao, M. Yue, Y. Hou, J. Han and M. Yang, *Acs Nano*, 2015, **9**, 2489-2501.
33. S. E, Q. Ma, J. Huang, Z. Jin and Z. Lu, *Composites Part A: Applied Science and Manufacturing*, 2020, **137**.
34. S. E, Q. Ma, D. Ning, J. Huang, Z. Jin and Z. Lu, *Composites Science and Technology*, 2021, **201**.
35. M. C. Vu, D. Mani, T.-H. Jeong, J.-B. Kim, C.-S. Lim, H. Kang, M. A. Islam, O. C. Lee, P. J. Park and S.-R. Kim, *Chemical Engineering Journal*, 2022, **429**.
36. Z. Liu, X. Fan, M. Han, H. Li, J. Zhang, L. Chen, Q. Zhu and J. Gu, *Chinese Journal of Chemistry*, 2023, **41**, 939-950.